



Published as: *Nature*. 2014 October 23; 514(7523): 518–522.

Structure and mechanism of Zn²⁺-transporting P-type ATPases

Kaituo Wang^{1,#,*}, Oleg Sitsel^{1,*}, Gabriele Meloni¹, Henriette Elisabeth Autzen¹, Magnus Andersson², Tetyana Klymchuk¹, Anna Marie Nielsen¹, Douglas C. Rees³, Poul Nissen¹, and Pontus Gourdon^{1,#,□}

¹Centre for Membrane Pumps in Cells and Disease - PUMPkin, Danish National Research Foundation, Aarhus University, Department of Molecular Biology and Genetics, Gustav Wieds Vej 10C, DK-8000 Aarhus C, Denmark

²Science for Life Laboratory, Department of Theoretical Physics, Swedish e-Science Research Center, KTH Royal Institute of Technology, SE-171 21 Solna, Sweden

³Division of Chemistry and Chemical Engineering and Howard Hughes Medical Institute, California Institute of Technology, Pasadena, California 91125, United States of America

Abstract

Zinc is an essential micronutrient for all living organisms, required for signaling and proper function of a range of proteins involved in e.g. DNA-binding and enzymatic catalysis¹. In prokaryotes and photosynthetic eukaryotes Zn²⁺-transporting P-type ATPases of class IB (ZntA) are crucial for cellular redistribution and detoxification of Zn²⁺ and related elements^{2,3}. Here we present crystal structures representing the phosphoenzyme ground state (E2P) and a dephosphorylation intermediate (E2.P_i) of ZntA from *Shigella sonnei*, determined at 3.2 and 2.7 Å resolution, respectively. The structures reveal a similar fold as the Cu⁺-ATPases with an amphipathic helix at the membrane interface. A conserved electronegative funnel connects this region to the intramembranous high-affinity ion-binding site and may promote specific uptake of cellular Zn²⁺ ions. The E2P structure displays a wide extracellular release pathway reaching the invariant residues at the high-affinity site, including Cys392, Cys394 and Asp714. The pathway closes in the E2.P_i state where Asp714 interacts with the conserved Lys693, which possibly stimulates Zn²⁺ release as a built-in counter-ion, as also proposed for H⁺-ATPases. Indeed, transport studies in liposomes provide experimental support for ZntA activity without counter-

Correspondence and requests for materials should be addressed to P.G. (pontus@sund.ku.dk).

[#]Current address: Department of Biomedical Sciences, University of Copenhagen, Blegdamsvej 3B, DK - 2200 Copenhagen, Denmark

[□]Current address: Department of Experimental Medical Science, Lund University, Sölvegatan 19, SE - 221 84 Lund, Sweden

* contributed equally

Author Contributions K.W., O.S., T.K. and A.M.N. cloned SsZntA constructs. K.W. and O.S. performed protein purification, crystallization and activity measurements in solution. G.M. conducted the vesicles studies, developed together with D.R.. K.W. processed the data and solved the crystal structures and all authors analyzed results. H.E.A and M.A. conducted MD simulations in the absence and presence of zinc, respectively. P.N and P.G. designed the project. K.W., O.S. and G.M. generated figures, P.N. and P.G. wrote the paper and all authors commented on the paper.

Atomic coordinates and structure factors for the *S. sonnei* ZntA (Q3YW59) E2-AlF₄⁻ and E2-BeF₃⁻ crystal structures have been deposited at the Protein Data Bank (PDB) under accession codes 4UMW and 4UMV.

Reprints and permissions information is available at www.nature.com/reprints.

The authors declare no competing financial interests.

Readers are welcome to comment on the online version of the paper.

transport. These findings suggest a mechanistic link between P_{IB}-type Zn²⁺-ATPases and P_{III}-type H⁺-ATPases, and show at the same time structural features of the extracellular release pathway that resemble the P_{II}-type ATPases such as the sarco(endo)plasmic reticulum Ca²⁺-ATPase^{4,5} (SERCA) and Na⁺,K⁺-ATPase⁶.

Zinc is an abundant transition metal in life, serving multiple functions¹. Yet elevated concentrations of Zn²⁺ are toxic, as are its heavy-metal mimetics such as Cd²⁺ and Pb²⁺ (Ref 7). Zn²⁺-transporting P-type ATPases (P_{IB,2}-ATPases, ZntA or CadA) are active transporters that are crucial for cellular detoxification of these elements³ as well as for sub-cellular redistribution of micronutritional zinc². The significance of Zn²⁺-ATPases is further underscored by the presence of multiple and occasionally redundant genes in higher plants². The lack of ZntA in animals, their prevalence in pathogens, and the fact that zinc is exploited in the host-microbe arms race, for instance to inactivate vital virulence determinants of *Streptococcus pneumoniae*⁸, make these P_{IB}-ATPases attractive targets for new antibiotics, antifungals and herbicides. ZntA couples ATP hydrolysis at the intracellular A- (actuator/dephosphorylation), P- (phosphorylation) and N-domains (nucleotide binding) to ion efflux through the transmembrane M-domain (Extended Data Fig. 1a). The mechanism is schematically described by the so-called Post-Albers cycle⁹ with four principal states, E1-E1P-E2P-E2 that define alternating access to an intramembranous high-affinity ion-binding site¹⁰ (Inset Fig 1a and Extended Data Fig. 1b). However, only structures of the related Cu⁺-transporting P_{IB}-ATPases CopA^{11,12} and a ZntA domain¹³ are available, limiting the functional and mechanistic understanding of this class of proteins. Fundamental questions that remain to be answered include how zinc transport is accomplished across the membrane and coupled to ATPase activity, and how sequence motifs that are specific to Zn²⁺-ATPases relate to structure and function.

We have determined the crystal structures of two reaction cycle intermediates of ZntA from *Shigella sonnei*, SsZntA, which is 99.2% identical to the *Escherichia coli* EcZntA (the best characterized member of the family) and stimulated by the equivalent ions *in vitro* (Fig. 1a and Extended Data Figs. 2, 3 & 4a). Crystals were obtained using a modified HiLiDe-technique¹⁴ (see Methods) and in the presence of the zinc chelator TPEN and either BeF₃⁻ or AlF₄⁻, mimicking the zinc-free phosphoenzyme ground state (denoted E2P) and a dephosphorylation intermediate (E2.P_i), respectively. The structures were determined at 3.2 and 2.7 Å resolution (Extended Data Table 1) and reveal a P_{IB}-type ATPase fold reminiscent of CopA with intracellular A-, P-, and N-domains, and eight similarly arranged transmembrane segments, MA, MB, and M1 through M6, albeit with shorter extracellular loops (Extended Data Fig. 5). The heavy-metal binding domain (HMBD), a characteristic feature of P_{IB}-ATPases (Extended Data Fig. 1a), was however not visible from the electron density maps, as was also the case for CopA¹¹. The intracellular domains are differently arranged in the two SsZntA structures, in agreement with the equivalent states of CopA and SERCA^{4,11,12}, i.e. with BeF₃⁻ mimicking the phosphorylation of Asp436 (SsZntA numbering throughout), which is buried and protected by the catalytic TGE-loop of the A-domain in this E2P like state, whereas the TGE-motif activates a water molecule coordinated to AlF₄⁻ imitating dephosphorylation at Asp436 as for a E2.P_i like state (Extended Data Fig. 6).

The single, intramembranous high-affinity Zn^{2+} site of ZntA¹⁰ deserves particular attention. Biochemical studies have indicated that Zn^{2+} -binding depends on Cys392 and Cys394 (in the CPC motif of M4), Lys693 (M5) as well as Asp714 (M6)^{10,15}. In the structures, the four residues overlap well with the equivalent cysteines, asparagine and methionine in the corresponding E2.P_i state of Cu⁺-ATPases¹¹ (Fig. 1b,c). Further supporting an important functional role of these four residues, the only other conserved side chains in the region that may participate in Zn^{2+} -binding are Met187 and Tyr354, but our mutations of these do not affect function (Fig. 2a). However, the Lys693 side-chain would be an unexpected ligand for Zn^{2+} (Refs 16,17) and indeed Zn^{2+} -binding is unaffected by the Lys693Ala mutation (Fig. 2b), suggesting that binding is rather established by the two cysteine thiolates and two oxygen ligands, possibly from Asp714 in a bidentate fashion; a recurrent coordination motif of Zn^{2+} -binding sites^{16,17}. Congruent with this role, the relative activity of the Asp714Glu mutant decreases with the increasing ionic radii and coordination distances of Zn^{2+} , Cd^{2+} and Pb^{2+} (Fig. 2a).

What is then the role of Lys693, which is also essential according to our mutational studies? A striking difference compared to CopA for the ion-binding region between M4, M5 and M6 is Asp714 in SsZntA. This side-chain is stabilized by Lys693 in the E2.P_i state (Fig. 3a and Extended Data Fig. 7a); an interaction of potentially important functional implications with the charge-stabilizing lysine possibly acting as a built-in counter-ion in zinc-free states (i.e. as observed here). Such a mechanism was earlier proposed for plasma-membrane H⁺-ATPases (Fig. 3c)¹⁸, and indeed residues Arg655 and Asp684 forming this pair in the *Arabidopsis thaliana* H⁺-ATPase AHA2 are located at almost overlapping positions of Lys693 and Asp714 of SsZntA¹⁸, pointing to common principles of ion transport in P_{IB}- and P_{III}-type ATPases.

Transport and putative proton countertransport were then analyzed in proteoliposomes. Whereas Zn^{2+} accumulated in the vesicles (Fig. 2c), we were unable to detect any changes in pH (Fig. 2d). As a positive control, the Ca²⁺-ATPase LMCA1 from *Listeria monocytogenes* showed clear proton antiport activity¹⁹ (Fig. 2d). Furthermore, while the electron density maps allowed identification of several water molecules in the E2-AlF₄⁻ structure, no sites were detected that could be ascribed to e.g. K⁺, Na⁺, Ca²⁺ or Mg²⁺ counter-ions, and these cations are also not required for ZntA activity (Extended Data Fig. 4b, see Methods for details). All considered, our observations thus support zinc flux without associated counter-ion transport.

In Cu⁺-ATPases, ion release has been proposed via a pathway lined by MA, M2 and M6 that remains open in the E2P and E2.P_i states¹². We were therefore surprised to learn that no extracellular pathway is evident in the E2.P_i state of SsZntA in contrast to CopA, and that instead substantial conformational changes occur in the M-domain in the E2P to E2.P_i state transition. These resemble on the other hand those of SERCA where a wide opening appears between M1-M2, M3-M4 and M5-M6 in the E2P state^{4,5}, and reseals in an occluded E2.P_i state (Fig. 3d and Extended Data Fig. 1). In ZntA the extracellular portions of M5-M6 shift away from the Zn^{2+} -binding CPC-motif, and rearrangements (less pronounced) are observed for M2 and M3-M4 that expose the high-affinity site to the extracellular side (Fig. 3d and Extended Data Fig. 7a). This SERCA-like pathway must allow for release of free zinc to the

extracellular environment, as further supported by an observed reorientation of the sulfur side-chains of the CPC-motif away from the ion-binding site between the E2P and E2.P_i states. With Lys693 being flexible without strong interaction to Asp714 in the E2P state (Fig. 3b), this hints at an additional role of Lys693 for electrostatic repulsion against re-entry of Zn²⁺, possibly further stimulated by Glu202 guiding Zn²⁺ to the extracellular environment. The equivalent residues of Glu202 in SERCA and CopA (Glu90 and Glu189, respectively) have been proposed to serve a similar purpose^{11,20} and supporting this notion, Glu202 is critical for function (Fig. 2a)²¹. Furthermore, Glu202 shows considerable conformational flexibility in a 60 ns molecular dynamics simulation of the open E2P structure, linking the intramembranous ion-binding site to the extracellular environment, as also supported by steered MD simulations of Zn²⁺ passage from the CPC-motif to the extracellular environment (Extended Data Fig. 7b–e).

How then is Zn²⁺ delivered to ZntA from the intracellular milieu in the first place? Although the current structures of Zn²⁺-free states are outward-oriented and therefore closed towards the intracellular side (Extended Data Fig. 1b), they hint at how Zn²⁺-entry may take place. The uptake of intracellular cations by P-type ATPases is expected to occur at the membrane interface at M1 (Refs 4,11,22,23), and in CopA through an entry site with an invariant methionine. Sequence analyses show that M1 in Zn²⁺-ATPases also harbor a conserved methionine (Met187) although located closer to the CPC-motif in ZntA (Fig. 1b,c & Extended Data Fig. 2), but mutational studies indicate that this residue alone is not essential (Fig. 2a). However, in contrast to CopA the entry area in Zn²⁺-ATPases displays a conserved and negatively charged funnel structure (lined by Glu184, Glu214 and Asp348 at the membrane interface) that stretches towards the intramembranous ion-binding site and which is plugged by Met187 and Phe210, the latter conserved as a phenylalanine/tyrosine in ZntA (Fig. 3e,f & Extended Data Fig. 8a & Extended Data Table 2). Whereas the activity of the Phe210Ala mutation is only moderately affected *in vitro*, the Met187Ala/Phe210Ala double mutation is inactive with reduced zinc binding compared to wild-type (Fig. 2a,b). We note that the equivalent residue to SsZntA Phe210 in H⁺-ATPases, Asn106, is a gatekeeper for proton entry (Fig. 3c)^{18,24}. With conformational changes anticipated for the shift to the E1 states, Zn²⁺ may thus be guided through the funnel and led directly to Cys392 of the high-affinity site, capped by Met148 and Phe210. Because the funnel is narrow and negatively charged, we find it likely that free Zn²⁺ ions and not a glutathione-ligated complex will interact with the funnel, thus unlike the proposed uptake mechanism of the heavy-metal ABC-exporter NaAtm1 (Ref 25).

The role of the HMBD of P_{IB}-ATPases is puzzling^{11,26,27}. In Cu⁺-ATPases, a platform formed by an amphipathic helix MB' at the intracellular membrane interface (Fig. 3g) has been proposed to serve as an interaction site for HMBDs as well as metal-donating chaperones for allosteric regulation and copper supply to the ATPase core. The MB' platform and its amphipathic character are maintained in ZntA, exposing several positively charged residues to the intracellular side (Fig. 3e,f and Extended Data Table 2). However, as no equivalent chaperones are known for zinc, the metal is most likely delivered by chelators such as glutathione, rendering the HMBD the most likely interaction candidate for the MB' platform in ZntA. Using a known structure of the almost identical HMBD of EcZntA¹³, the

ClusPro docking server docks the domain immediately at MB', stabilized by charge complementation (as was also proposed for CopA^{27,28}) with the metal-binding CXXC-motif solvent-accessible in the vicinity of the entry funnel (Extended Data Fig. 8b–d). Truncations and mutations of the HMBD retain a functional ZntA, only with reduced activity (Refs 15,29 and Fig. 2a), and we therefore favor an autoregulatory role for the domain.

The first atomic structures of a Zn²⁺-transporting P_{IB}-type ATPase reveal unique features such as an intracellular, negatively charged and presumably ion-catching funnel, a high-affinity site with a putative lysine switch acting as a built-in counter-ion with an unexpected similarity to P_{III}-type plasma membrane H⁺-ATPases, and an extracellular Zn²⁺-release pathway, which unlike for copper-transporting P_{IB}-type ATPase resembles that of the classical P_{II}-type ion pumps. These findings significantly increase our understanding of zinc transport in cells (Fig. 4), and represent new possibilities for biotechnology and biomedicine. Detailed insight into the transport mechanism and specificity determinants may for example aid in using plant biotechnology to accumulate valuable zinc in edible plants or to decontaminate soil from heavy metals, and the release pathway may serve as a favorable target site for new antibiotics.

Methods

Protein expression and purification

Several ZntA homologues from different prokaryotes were cloned and tested for expression, purification and crystallization in a parallel approach. SsZntA (Q3YW59) was cloned into pET52 with a C-terminal hexa histidine-tag and transformed into the C41(DE3) *E. coli* expression strain. Cells were grown in LB medium at 37 °C to OD₆₀₀=1.0, the shaker flasks cooled for 30 minutes with ice-water, and then induced with 1 mM IPTG (final concentration) at 20 °C for 20 hours. Harvested cells were resuspended with TKG buffer (17 g cells per 100 mL buffer) containing 20 mM Tris-HCl pH=7.5, 200 mM KCl and 20 % v/v Glycerol and frozen at –20 °C. Prior to cell rupture, the solution was added (final concentrations) 5 mM MgCl₂, 5 mM β-mercaptoethanol (BME), 2 ug/mL DNaseI, 1 mM phenyl-methane-sulfonyl-fluoride and Roche protease inhibitor cocktail (1 tablet per 200 mL) and the cells opened using a high pressure homogenizer (three runs at 15,000–20,000 psi). The sample was then kept at 4 °C throughout the entire purification procedure until crystallization. Cell debris was removed by centrifugation at 23,000 g for 20 minutes and membranes isolated by ultracentrifugation at 250,000 g for 3 hours. The membrane pellet was resuspended in 20 mM Tris-HCl pH=7.5, 200 mM KCl, 20 % v/v Glycerol, 5 mM MgCl₂ and 5 mM BME, to a final concentration 12 mL buffer per gram membrane and then subjected to 10 mg/mL (final concentration) octaethylene-glycol-monododecyl-ether (C₁₂E₈) for 1 hour with gentle stirring. Unsolubilized material was removed by ultracentrifugation at 250,000 g for 30 minutes. The supernatant was supplemented with imidazole and solid KCl (final concentrations of 50 and 500 mM), filtered (0.22 μm) and then applied to several sequential 5 mL pre-packed Ni²⁺-chelating columns (HisTRAP™ HP from GE Healthcare, material from four liters of cells per column). The columns were washed with buffer containing 20 mM Tris-HCl pH=7.5, 200 mM KCl, 20 % v/v Glycerol, 5 mM MgCl₂, 5 mM BME, 0.15 mg/mL C₁₂E₈ and 50 mM imidazole until UV absorption

reached the baseline and elution achieved with an additional 450 mM imidazole (final concentration). SsZntA containing fractions were pooled, the protein concentrated to 20 mg/mL and then subjected to size-exclusion chromatography. 50 mg were injected into a XK16/100 column prepared with 100 mL column volume Superose 6 Prep Grade (GE Healthcare) equilibrated with 20 mM MOPS-KOH pH=6.8, 80 mM KCl, 20 % v/v Glycerol, 5 mM MgCl₂, 5 mM BME and 0.15 mg/mL C₁₂E₈ and the resulting main peak was pooled and concentrated to 12 mg/mL, aliquoted, flash frozen in liquid nitrogen and stored at -80 °C. Yields exceeded 10 mg purified protein per liter of *E. coli* cell culture. Final protein purity was monitored using SDS-PAGE and the protein concentration was assessed using UV₂₈₀ absorption.

Crystallization

SsZntA aliquots were thawed and supplemented with 4 mg/mL (final concentration) C₁₂E₈ and incubated without stirring for 16 hours at 4 °C reaching a modified HiLiDe condition¹⁴. The sample was then ultracentrifuged at 100,000 g for 10 minutes and diluted to a final concentration about 6–8 mg/mL protein and treated with 10 mM NaF, 2 mM AlCl₃ or BeSO₄, 2 mM EGTA, and 10 μM N,N,N',N-tetrakis-2-pyridylmethyl-ethylenediamine (final concentrations) for 30 minutes. Crystals were grown using the hanging drop vapor diffusion method at 19 °C. The best SsZntA E2-AlF₄⁻ crystals were grown using a reservoir with 300 mM lithium acetate, 3% v/v t-BuOH, 14 % Poly ethylene glycol 2000 monomethyl ether (PEG2000-MME), 7 % v/v Sorbitol, 10 % v/v Glycerol and 5 mM BME. In contrast, the best SsZntA E2-BeF₃⁻ crystals were obtained using a reservoir with 100 mM MgCl₂, 200 mM lithium acetate, 17 % v/v PEG2000-MME, 10 % v/v glycerol and 5 mM BME. More than 1000 crystals were fished with litho-loops and flash cooled in liquid nitrogen and tested at synchrotron sources. The final datasets were collected at SLS, Villigen, Switzerland, using the X06SA beamline and a wavelength of 1.0000 Å (0.9787 Å for Se-E2.P_i[AlF]), a temperature of 100 K and a pixel detector (Pilatus 6M).

Data processing and structure determination

Data were processed and scaled with XDS³¹ to 2.7 Å and 3.2 Å resolution, respectively. The E2-AlF₄⁻ and E2-BeF₃⁻ crystals belonged to space group C222₁ and P2₁, respectively. Initial phases for the E2-AlF₄⁻ form were obtained with molecular replacement (MR) using PHASER³² and monomer A of LpCopA (PDB-ID 3RFU, Ref 11) as a search model. Anomalous peaks for a Se-SAD dataset of the E2-AlF₄⁻ form were calculated using the MR phases, and the Se-Met positions were used to guide model building. Model building was performed with COOT³³, using the LpCopA structure as a template. Model refinement was carried out using phenix.refine³⁴, applying TLS parameters in the late stages of refinement only, reaching R_{cryst}/R_{free} values of 20.7/24.0 and 21.0/28.1, respectively. The E2-BeF₃⁻ form was also determined by MR using the refined SsZntA E2-AlF₄⁻ structure as a search model and refined using a similar procedure. The final refinement statistics are listed in Extended Data Table 1. Structures were analyzed using Molprobit, indicating that 96.35/94.42, 3.49/5.08 and 0.17/0.51 % of the residues were in the favored, allowed and non-favored region, with 6.64/10.91 % rotamer outliers and 6.48/10.11 as clash scores respectively for the E2.P_i and E2P states.

Functional characterization

The purification protocol for functionally assessed SsZntA constructs were similar to the one described for crystallization (HMBD lacks the first 103 residues). However, following affinity-chromatography, the samples were treated with 1 mM EDTA and then subjected to a 5 mL HiTRAP desalting column (GE Healthcare) using the equivalent SEC-buffer as for crystallization. Release of inorganic phosphate associated with ATPase activity was assessed using the so-called Baginski assay³⁵. The reaction system contained 5 µg protein, 40 mM MOPS-KOH pH=6.8, 150 mM NaCl, 5 mM KCl, 5 mM MgCl₂, 3.0 mg/mL C₁₂E₈, 1.2 mg/mL soybean lipid, 20 mM cysteine, 5 mM NaN₃ and 0.25 mM Na₂MoO₄ in a total volume of 50 µL. This solution was first incubated with different types of heavy metal ions or EGTA, supplemented with 3 mM ATP (final concentration) to start the reaction and then incubated for 10 minutes while shaking in 37 °C. 50 µL of freshly prepared stop solution (2.5 % w/v ascorbic acid, 0.4 M v/v HCl, 0.48 % w/v (NH₄)₂MoO₄, 0.8 % SDS) was then added to stop the reaction and start color development. After 10 minutes incubation at 18 °C, 75 µL colorimetric solution (2 % w/v arsenite, 2 % v/v acetic acid and 3.5 % w/v sodium citrate) was added to the mixture and incubated for another 30 minutes at 18 °C. Absorbance was measured at 860 nm. One experiment with three replicates was performed for each construct and ion.

Reconstitution in proteoliposomes

E. coli polar lipids (25 mg/mL) and egg-yolk phosphatidyl choline (25 mg/mL) in chloroform were mixed at a 3:1 ratio (w/w) and dried under a nitrogen stream and continuous rotation to form a homogeneous thin film in a glass balloon. Lipids were desiccated overnight under vacuum (protected from light) and suspended in 1 mM DTT to a final concentration of 25 mg/mL. A concentrated stock (10x) was used to bring the suspension to final 20 mM MOPS pH=6.8, 250 mM NaCl and 1 mM DTT. Lipids were subjected to three rounds of freeze-thawing in liquid N₂. Proteoliposomes were prepared by extrusion (11 times) through 0.2 µm polycarbonate filters to form large unilamellar vesicles (LUVs) using a mini extruder (Avanti Polar Lipids) equipped with two 1 mL gas-tight syringes. Proteoliposomes were destabilized by addition of n-dodecyl-β-D-maltoside (DDM) to final 0.02 % (w/v) and tilting for one hour at 18 °C, and subsequently placed on ice for 10 minutes. Wild-type and Asp436Asn SsZntA as well as LMCA1 (1–2 mg/mL, purified essentially as described for crystallization) was added to a final protein-to-lipid ratio of 1:20 (w/w) and the mixture was incubated for 1 h at 4°C under tilting. Control liposomes were prepared using the same procedure without addition of protein. Detergent was removed through consecutive incubations with activated Bio-Beads SM-2 (BioRad), by exchanging the beads after 1, 16, 18 and 20 hours. Biobeads were subsequently removed, proteoliposomes collected by ultracentrifugation at 163,000 g for 45–60 minutes at 4 °C, and resuspended in 20 mM MOPS pH=6.8, 250 mM NaCl, 1 mM DTT (Buffer PL) to a final protein concentration of 1 mg/mL.

Zinc transport assays using FluoZin-1

Wild-type and Asp436Asn SsZntA proteoliposomes were diluted 1:2 in 20 mM MOPS pH=6.8, 250 mM NaCl, 1 mM DTT to a protein concentration of 0.5 mg/mL. A stock of the

fluorescent Zn²⁺ chelator FluoZin-1 (2 mM in H₂O) was added to a final concentration of 200 μM. FluoZin-1 encapsulation was performed by three freeze-thaw cycles and subsequent extrusion through 0.2 μm polycarbonate filters. Proteoliposomes were collected by ultracentrifugation at 163,000 g for 45–60 minutes at 4 °C, and the supernatant containing excess FluoZin-1 removed. Proteoliposomes were washed with 1 mL of Buffer PL, collected by ultracentrifugation and suspended in the same buffer (1 mL). Transport assays were performed in the presence of final 10 mM MgCl₂ on 100 μL samples. Reaction was initiated by addition of concentrated stocks of ZnCl₂ (1mM) and ATP (10 mM) stock to final 40 μM ZnCl₂ and 1 mM ATP. A fluorescence time-course was measured in a 96-well plate reader using an excitation wavelength of 485 nm and emission wavelength of 520 nm. Experiments in the absence of ATP were performed in parallel as control. The ATP-dependent Zn²⁺ transport was determined as F/F_0 , where F is the difference between the fluorescence measured in the presence and the absence of ATP, and F_0 is the fluorescence recorded immediately after ATP addition. Each condition was tested at least in duplicates and one representative trace is shown for each.

H⁺ counter-ion transport assays using Pyranine

SsZntA (wild-type) and LMCA1 and control (proteo)liposomes were diluted 1:2 to final 20 mM MOPS pH=7.0, 250 mM NaCl, 100 mM KCl, 10 mM MgCl₂ and 1 mM DTT (Buffer Counter). A stock of the fluorescent pH-indicator pyranine (0.1 M in H₂O) was added to final 10 mM. Pyranine encapsulation was performed by three freeze-thaw cycles and subsequent extrusion through 0.2 μm polycarbonate filters. Proteoliposomes were collected by ultracentrifugation at 163,000 g for 45–60 minutes at 4 °C and the supernatant removed. Proteoliposomes were washed with 1 mL of Buffer Counter, collected by ultracentrifugation and suspended in the same buffer. Reaction was initiated by addition of concentrated stocks of ZnCl₂ (1mM) or CaCl₂ (2.5mM) and ATP (10 mM) to obtain final 40 μM ZnCl₂ (for SsZntA) or 100 μM CaCl₂ (for LMCA1), and 1 mM ATP. Experiments in the absence of ATP were performed in parallel as well as experiments on control liposomes. A fluorescence time course was measured in a 96-well plate reader using an excitation wavelength of 450 nm and emission wavelength of 520 nm. The ATP-dependent H⁺ counter-ion transport was determined as F/F_0 where F is the difference between the fluorescence measured in proteoliposomes and in control liposomes and F_0 is the fluorescence recorded immediately after ATP addition. Each condition was tested at least in duplicates and one representative trace is shown for each.

Effect of Na⁺ or K⁺ on SsZntA activity

To investigate the effect of Na⁺ or K⁺ on the activity of wild-type SsZntA in detergent micelles, the buffer in SsZntA stock solutions was exchanged using 5 mL HiTrap desalting columns packed with Sephadex G-25 resin to K⁺ depleted (20 mM MOPS pH=6.8, 250 mM NaCl, 1 mM DTT, 0.01 mg/mL and C₁₂E₈, 20 % glycerol) or Na⁺-depleted solutions (20 mM MOPS pH=6.8, 250 mM KCl, 1 mM DTT, 0.01 mg/mL C₁₂E₈ and 20 % v/v glycerol). To exchange the buffer in proteoliposome preparations, 100 μL stocks were diluted in 1 mL of 20 mM MOPS pH=6.8, 250 mM NaCl and 1 mM DTT or 20 mM MOPS pH=6.8, 250 mM KCl and 1 mM DTT, collected by ultracentrifugation, washed with 1 mL of the corresponding buffer and regenerated by three freeze-thaw cycles. This procedure has been

repeated and the obtained proteoliposomes suspended in a final volume of 100 μ L. The ATPase activity was determined using the Baginski method described above in the presence of final 40 μ M ZnCl₂ or 1 mM EDTA for background correction. One experiment with three replicates was performed for each of the ion tested (Na⁺, K⁺).

Effect of Mg²⁺ on SsZntA activity in proteoliposomes

The buffer was exchanged by diluting proteoliposomes stocks in 20 mM MOPS pH=6.8, 250 mM NaCl, 80 mM KCl, 5mM MgCl₂, 1 mM DTT (Buffer MCA) or 20 mM MOPS pH=6.8, 250 mM NaCl, 80 mM KCl, 1 mM DTT (Buffer MCB) followed by three freeze-thaw cycles and extrusion through 0.2 μ m polycarbonate filters. Proteoliposomes were collected by ultracentrifugation at 163,000 g for 60 minutes at 4 °C and suspended in the corresponding buffer. The ATPase activity was determined using the Baginski method as described above. As the buffer utilized in assays contains ATP and MgCl₂ (required for ATP hydrolysis), ATPase activity is stimulated exclusively for correctly oriented ssZntA (N-domain facing outside). The presence or absence of Mg²⁺ in proteoliposome lumen (buffer MCA or MCB) allows identifying the putative requirement of Mg²⁺ counter-transport for activity. One experiment with three replicates was performed.

Determination of Zn²⁺-binding stoichiometry using Zincon

SsZntA and mutants were titrated with 5–6 ZnCl₂ equivalents/mol (using a 10 mM ZnCl₂ stock) and subsequently desalted in 20mM MOPS-KOH, pH=6.8, 80 mM KCl, 100 mM NaCl, 3mM MgCl₂, 0.15 mg/ml C₁₂E₈, 1 mM TCEP using a Hi-Trap desalting column (GE Healthcare) packed with Sephadex G-25 resin to remove free or loosely bound metal. Zn²⁺ content in the samples was determined by colorimetric quantification upon complex formation with 2-[5-(2-hydroxy-5-sulfophenyl)-3-phenyl-1-formazyl]benzoic acid (Zincon). Briefly, metal release was achieved upon incubation in a final concentration of 30 mM HCl. Subsequently samples were diluted to a final concentration of 100 mM borate, pH=9, 4 M guanidinium chloride followed by addition of Zincon to a final concentration of 40 μ M. The quantification of Zincon-Zn²⁺ complex was performed on a 96-well plate reader (Perkin Elmer) by measurement of the absorbance at 630 nm using a calibration curved obtained by addition of increasing amount of ZnCl₂ in the same buffer. Protein concentration was determined by a modified Bradford assay. 10 μ l protein solutions were incubated with 10 μ l of 1 M NaOH. Subsequently 500 μ l Bradford reagent was added and quantification performed on a 96-well plate reader (Perkin Elmer) by measurement of the absorbance at 600 nm using a calibration curved obtained with BSA standards. Three independent experiments with three replicates for each experiment were conducted.

ClusPro docking

SsZntA in the E2P state and the *E. coli* ZntA HMBD fragment containing residues 46–118 (PDB-ID 1MWY, Ref 13) was chosen. Sequence identity to corresponding residues of the SsZntA HMBD was 97 %. Docking was done using the ClusPro server³⁶. The best model in the van der Waals + electrostatics scoring scheme was selected, as judged by cluster size scores.

Molecular dynamics simulations

Two 60 ns of atomistic molecular dynamics (MD) simulation were run; one of each of the two ZntA structures. The AlF_4^- bound in the E2.P_i structure was modeled as H_2PO_4^- as described previously³⁷. The Asp436-BeF₃⁻ in the E2P structure was modeled as a phosphorylated aspartate utilizing CHARMM27 parameters³⁸. The bound magnesium ion was retained in both structures. ZntA was embedded in a DOPC membrane based on coordinates of a pre-equilibrated slab multiplied eight times from the Laboratory of Molecular & Thermodynamic Modeling and the proteins were positioned according to transmembrane alignment with the Orientations of Proteins in Membranes database coordinates of the E2.P_i Cu⁺-ATPase structure (PDB-ID 3RFU, Ref 11)³⁹. Lipids comprising atoms within 0.8 Å of any protein atom were deleted. Finally, the protein-membrane systems were further solvated with TIP3P water and neutralized with sodium.

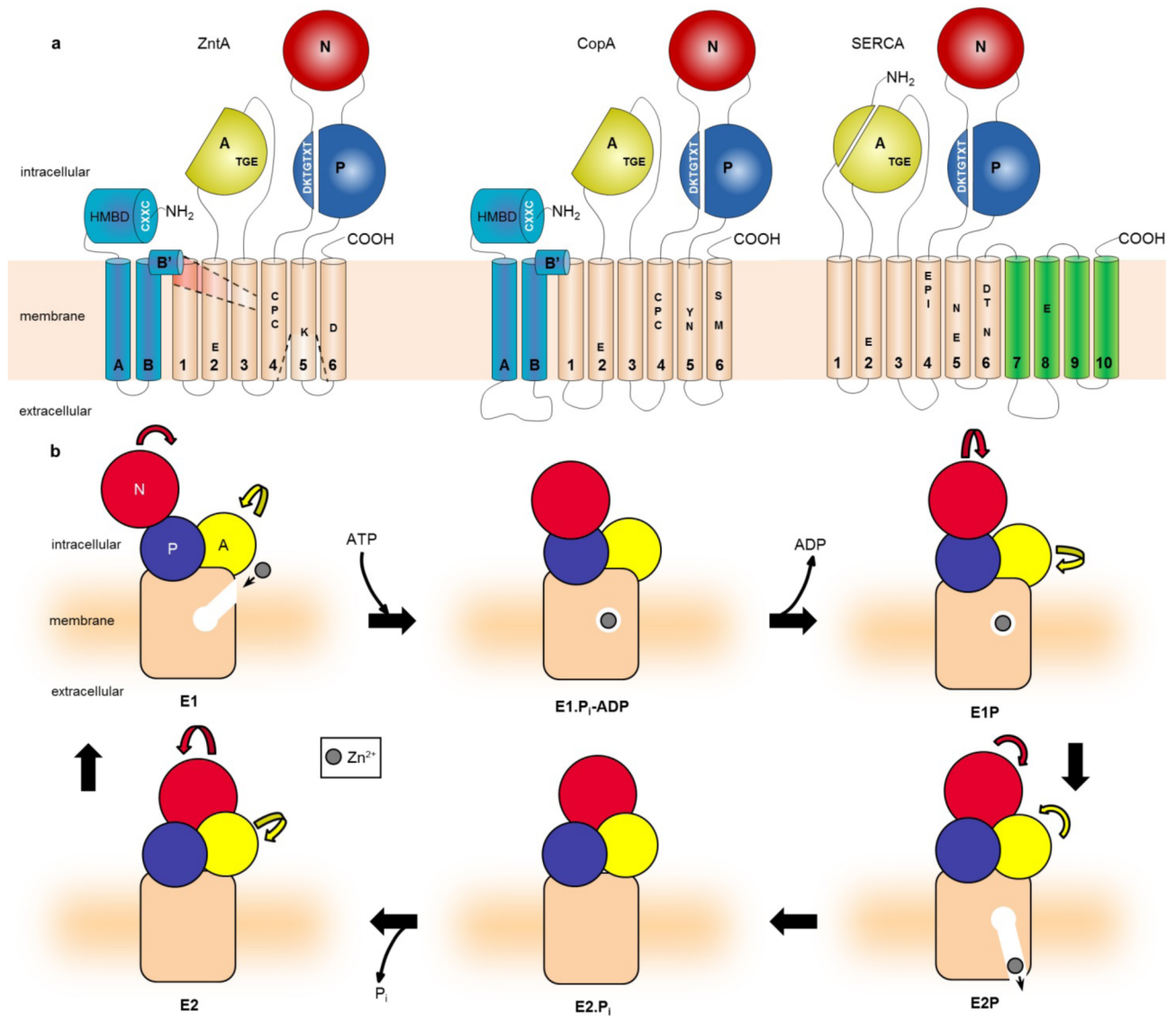
MD simulations were run using the NAMD 2.8 program⁴⁰ employing the CHARMM27 force field for proteins⁴¹ and the CHARMM36 force field for lipids⁴². Prior to simulation, the systems were subjected to 2,000 steps of conjugate gradient minimization. Then followed a 0.5 ns MD simulation where everything but the lipid tails was kept constant (NVT ensemble, T = 298 K), allowing the lipids to adapt to the protein to some extent. Next, the systems were minimized for 1,000 steps after which all atoms were allowed to move freely for 0.5 ns (NPT ensemble, T = 298 K, P = 1 atm) except for the protein back bones which were held fixed. Finally, all atoms were allowed to move freely in a production run of 60 ns. The temperature was controlled by Langevin dynamics and the Nosé-Hoover Langevin piston method was used for controlling the pressure^{43,44}. Electrostatics was fully accounted for by applying the Particle Mesh Ewald method with periodic boundary conditions⁴⁵. The van der Waals interactions were truncated at 12 Å, applying a switching function at 10 Å. The neighbor-list containing all pairs of atoms for which non-bonded interactions is calculated, included atoms within 14 Å of each other and was updated for every 20 steps. Bonded interactions were evaluated every 1 fs, while electrostatic and vdW interactions were evaluated every 4 and 2 fs, respectively. Each production run was run for 60 ns, producing 60,000 frames of which 2,000, evenly spread over the simulation time, were used for analysis.

To describe the release pathway and accompanying Zn²⁺-protein interactions, a steered MD (SMD) approach was used^{46,47}. A divalent zinc ion was placed between ion-coordinating residues Cys392, Cys394 and Asp714 in the E2P state followed by deletion of three clashing water molecules and a 10,000-step conjugate-gradient energy minimization. A force constant of 5 kcal/mol/Å² and velocities ranging from 10 to 20 Å/ns were applied to the ion directed from the inside out in the z-direction in ten independent 1 ns simulations. Similar release pathways were observed in the ten SMD simulations and the number of Zn²⁺-protein interactions within a 5 Å cut-off were calculated. The C_α's of 6 remote residues (148, 198, 367, 383, 385 and 705) were restrained to keep the system from drifting when applying the force.

Figures

Structural representations were generated using Pymol⁴⁸. Helices MA, MB, and MB' have been removed for clarity in Fig. 1b,c and helices M3-M4 of LpCopA and SsZntA were aligned for generation of Fig. 1c. In Fig. 3c, the structures are aligned using the M4-M6 transmembrane helices and the view is from the extracellular side. Taking the E1-E2 conformational changes into account, Lys693-Asp714 (SsZntA) and Arg655-Asp684 (AtAHA2) almost overlap. In H⁺-ATPases, AtAHA2-Asp684 participates in proton transfer to the extracellular side and Arg655 has been proposed to stimulate proton release from Asp684 and prevent re-protonation¹⁸. Phe210 of SsZntA separates the electronegative ion entry funnel from the membranous Zn²⁺ site and overlaps with AtAHA2-Asn106, which stabilizes the protonated AHA2-Asp684 (Ref 18) and blocks intracellular proton exchange²⁴. In Fig. 3d, electron density is provided for the E2P state. A deep pathway reaches the intramembranous high-affinity ion-binding site and may allow Zn²⁺-release via Glu202. In Fig. 3e the view is from the intracellular side. Ion entry to SsZntA may occur through negatively charged residues placed inside the periphery of positively charged residues of MB'. The view of Fig. 3f is identical to the one of Fig. 3e displaying a highly electronegative funnel (negative surface in red, positive in blue) formed by residues of M1, M2 and M3. The funnel extends towards the ion-binding CPC-motif and is constricted by Met187 and Phe210, presumably guiding ions to the membranous high-affinity ion-binding site and excluding non-transported compounds. See also Extended Data Table 2b. The view of Fig. 3g is identical to the one of Fig. 3e of the Cu⁺-ATPase LpCopA (PDB-ID 3RFU, Ref 11) where ion uptake instead has been proposed through a transient Cu⁺-binding site.

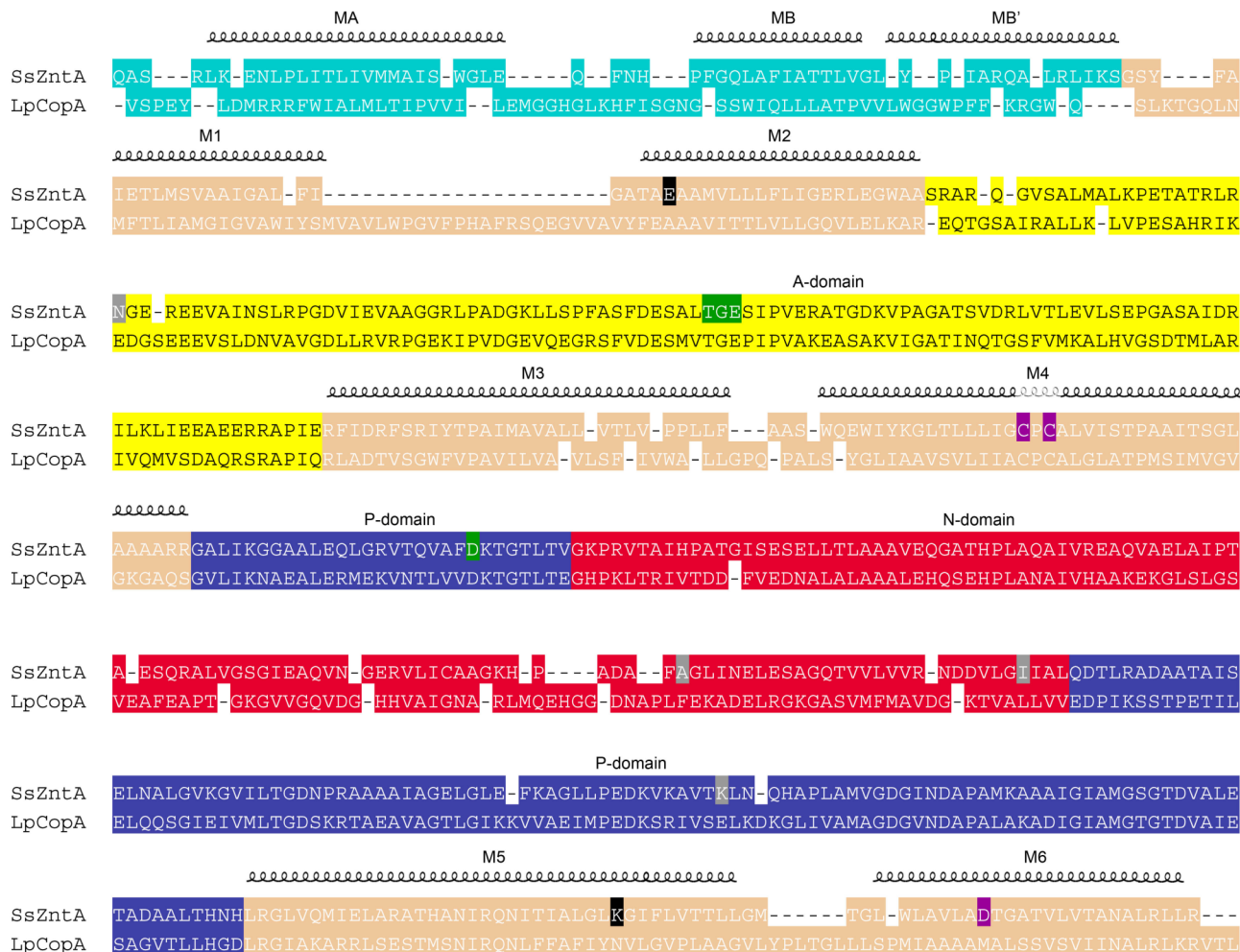
Extended Data



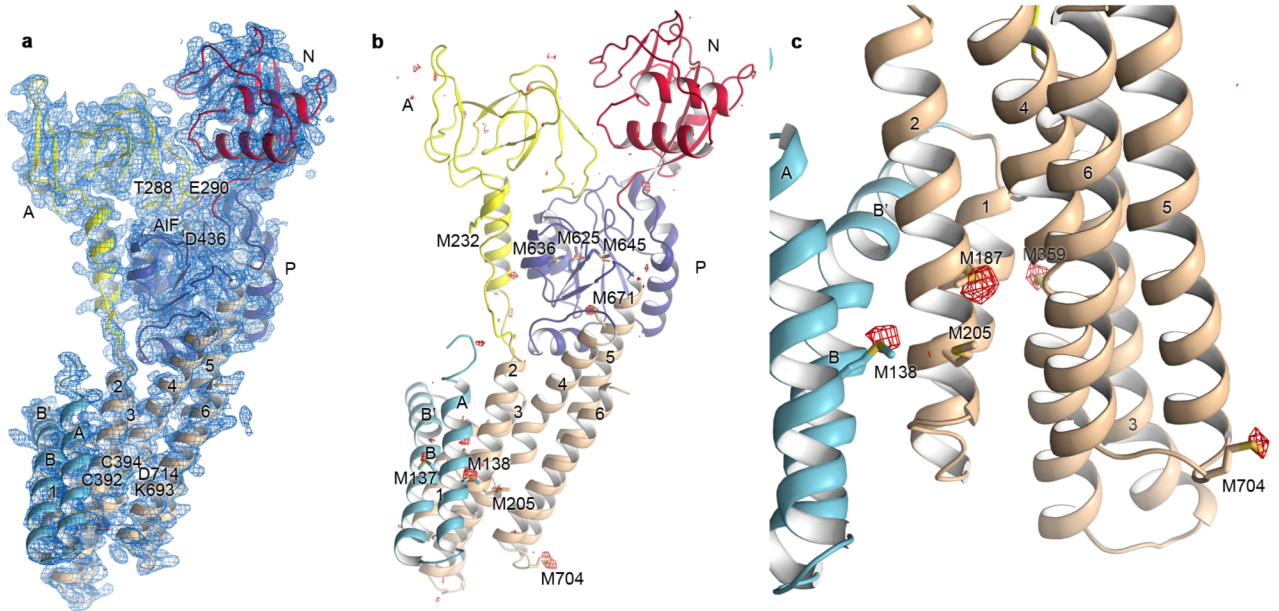
Extended Data Figure 1. Topology and reaction cycle of P-type ATPases

a, Topology of ZntA, CopA, and SERCA. Key residues in the HMBD, A-, P-, N- and M-domains are highlighted. In ZntA, the negatively charged ion entry funnel and release pathway are outlined. Asp436 in SsZntA is the the autophosphorylated/dephosphorylated catalytic aspartate in the DKTGTXT-motif of the P-domain. Cys392 and Cys394 in M4, Lys693 in M5 and Asp714 in M6 of SsZntA have been proposed to bind zinc in biochemical studies^{10,15,49}. **b**, The Albers-Post (E1-E2) reaction cycle of Zn^{2+} -transporting P-type ATPase^{9,50}. Phosphorylation events in the intracellular domains drive large conformational changes that permit alternating access to transport sites in the membrane about 50 Å from the ATP-targeted catalytic aspartate. According to the model, a high-affinity state (E1), open to the intracellular space, binds a Zn^{2+} and enters an occluded state, which then undergoes phosphorylation. Completion of this event (E1P) triggers release of the ion establishing an

outward-facing, low-affinity state (E2P). Release of inorganic phosphate yields the fully dephosphorylated conformation (E2), which is followed by restoration of the inward-facing conformation (E1) that initiates a new reaction cycle.

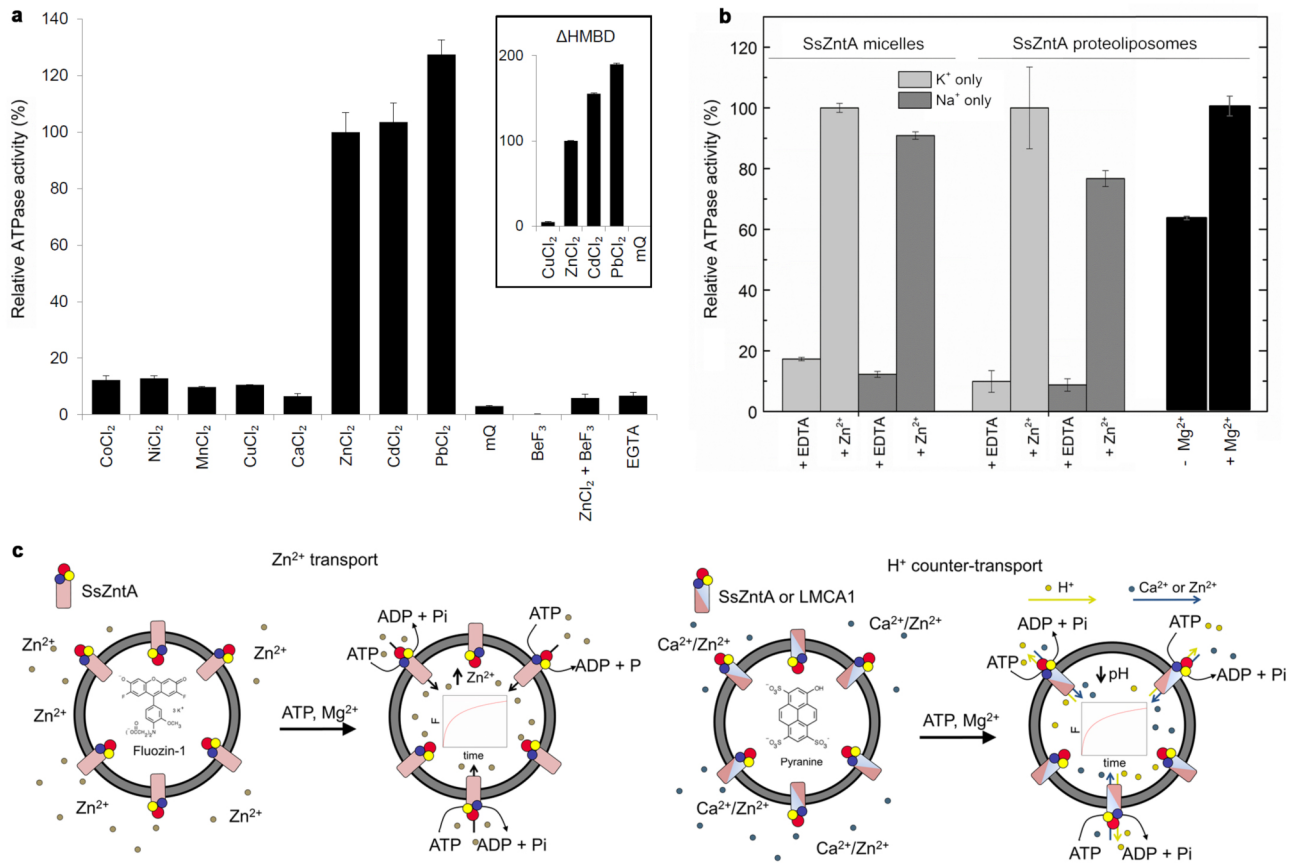


Extended Data Figure 2. Structure-based sequence alignment of SsZntA and LpCopA
 Helix positions are indicated for SsZntA, and noteworthy residues are highlighted. Four of seven likely functionally irrelevant amino acid positions in which ZntA from *Shigella sonnei* and *Escherichia coli* differ are highlighted in grey. The high-affinity ion-binding Cys392, Cys394 and Asp714 are indicated in purple, the catalytically phosphorylated aspartate and the dephosphorylating TGE motif are highlighted in green. Glu202 and Lys693, possibly related to ion release, are marked in black. The alignment was performed using SALIGN⁵¹.



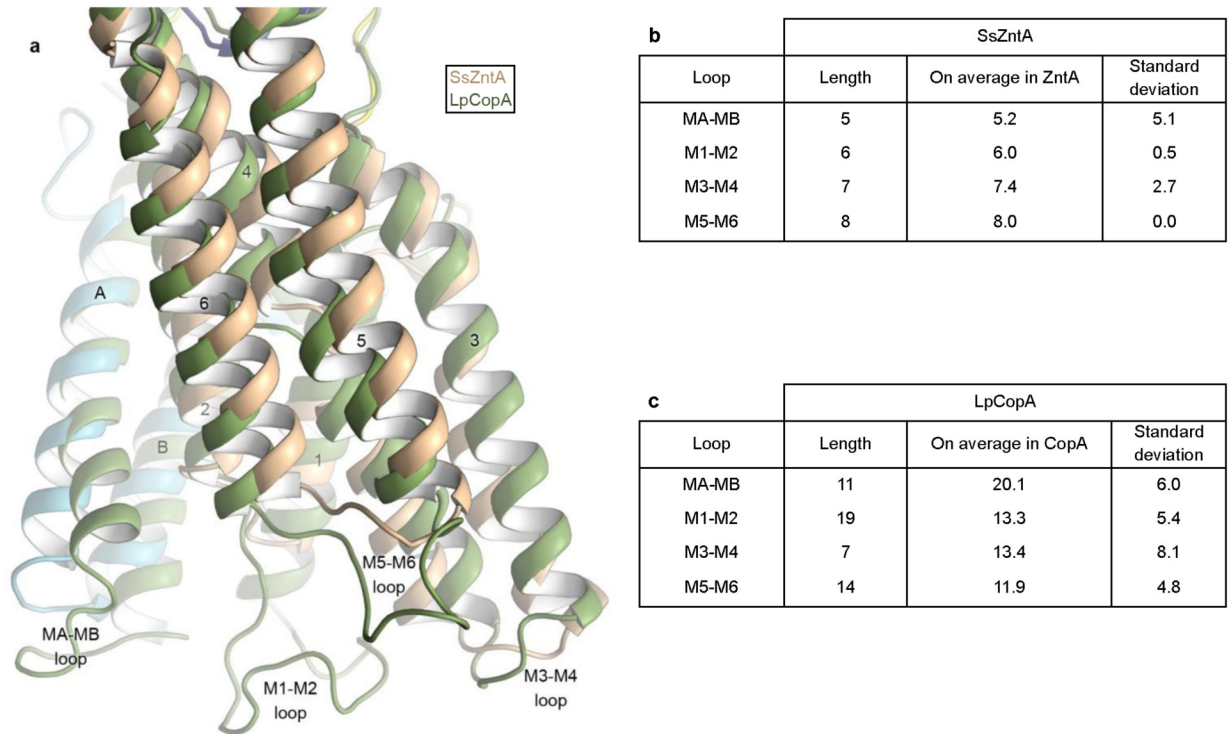
Extended Data Figure 3. Electron density of the determined E2.P_i state of SsZntA

a, Final $2F_o - F_c$ electron density of SsZntA in the E2.P_i state. The density is contoured at 1σ and the view is equivalent to Fig. 1a. **b–c**, Se-Met peaks calculated using Se-SAD data and phases obtained from molecular replacement guided model building. The anomalous difference Fourier map is contoured at 3σ . **b**, View of the entire protein. **c**, View of the M-domain.



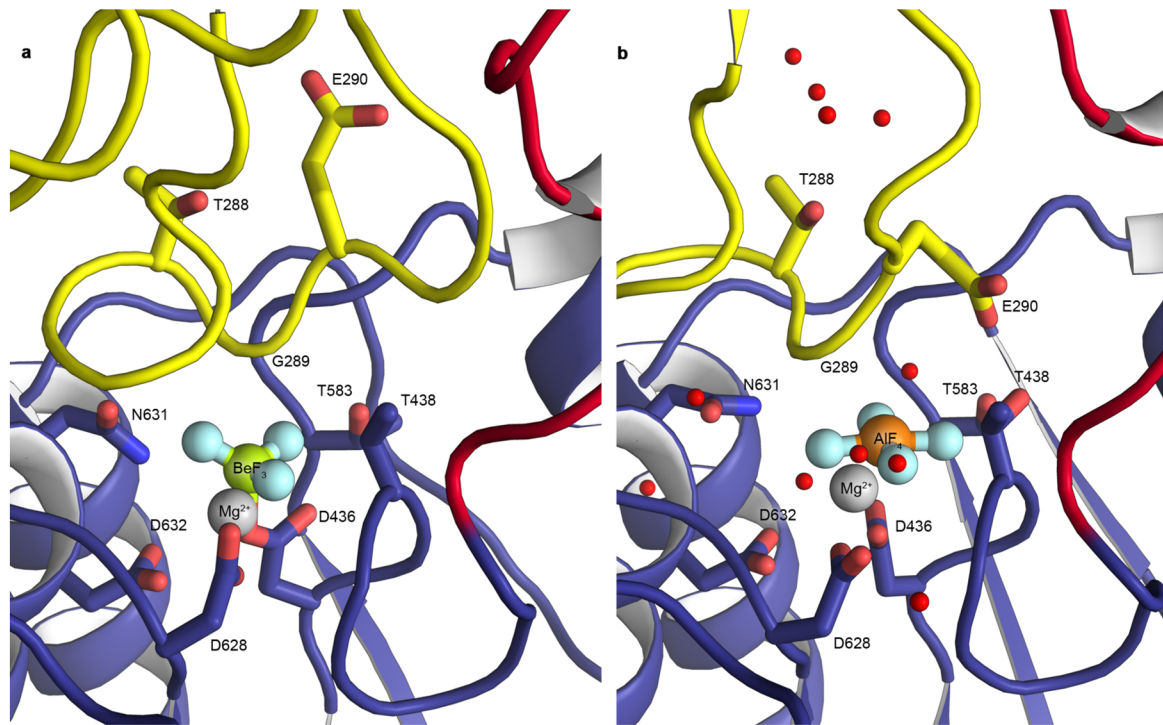
Extended Data Figure 4. Functional assays of SsZntA

a, Wild-type and Δ HMBD (inset) SsZntA ATPase activity is stimulated by Zn²⁺, Cd²⁺ and Pb²⁺. ATPase activity (normalized, with the activity in the presence of Zn²⁺ as 100 % for wild-type and Δ HMBD, respectively) was determined using the Baginski assay (see methods for details). This ion stimulation profile matches the one observed for ZntA from *E. coli*⁵². Technical average and s.d. (n=3). **b**, Effect of K⁺, Na⁺ and Mg²⁺ on SsZntA activity. ATPase activity of wild-type SsZntA in detergent micelles or upon reconstitution in proteoliposomes, in buffers containing exclusively Na⁺ or K⁺ as determined by the Baginski assay. For Mg²⁺ the activity was in proteoliposomes with internal buffers with or without MgCl₂. Technical average and s.d. (n=3). **c**, Zn²⁺ and H⁺ transport across vesicle membranes. Zinc transport of wild-type and Asp436Asn SsZntA proteoliposomes, respectively, monitored using the zinc-selective chelator FluoZin-1 (left). Proton counter-ion transport in wild-type SsZntA or Ca²⁺-ATPase LMCA proteoliposomes, respectively, monitored using the pH indicator pyranine (right).



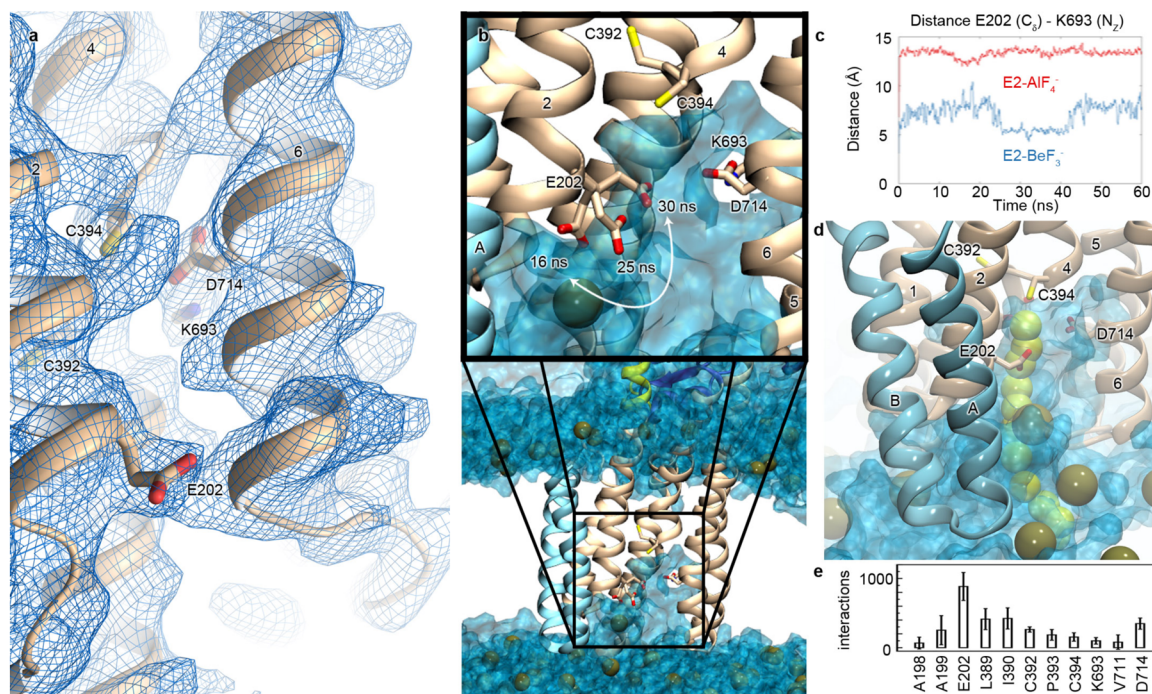
Extended Data Figure 5. Structural comparison of P-type ATPases

a, Difference between the extracellular loops of SsZntA and LpCopA. SsZntA is colored as in Fig. 1a and LpCopA in dark green and the proteins have been aligned on helices M5-M6. Note that the loops are substantially longer in LpCopA than in SsZntA, a conserved difference between Cu^+ - and Zn^{2+} -transporting P-type ATPases (see also panel b). **b,c** Comparison of the extracellular loop lengths of ZntA (b) and CopA (c). The lengths of the loops in SsZntA and LpCopA are shown as well as averages based on 521 and 617 proteins (with less than 99 % and 95% sequence identity, respectively).



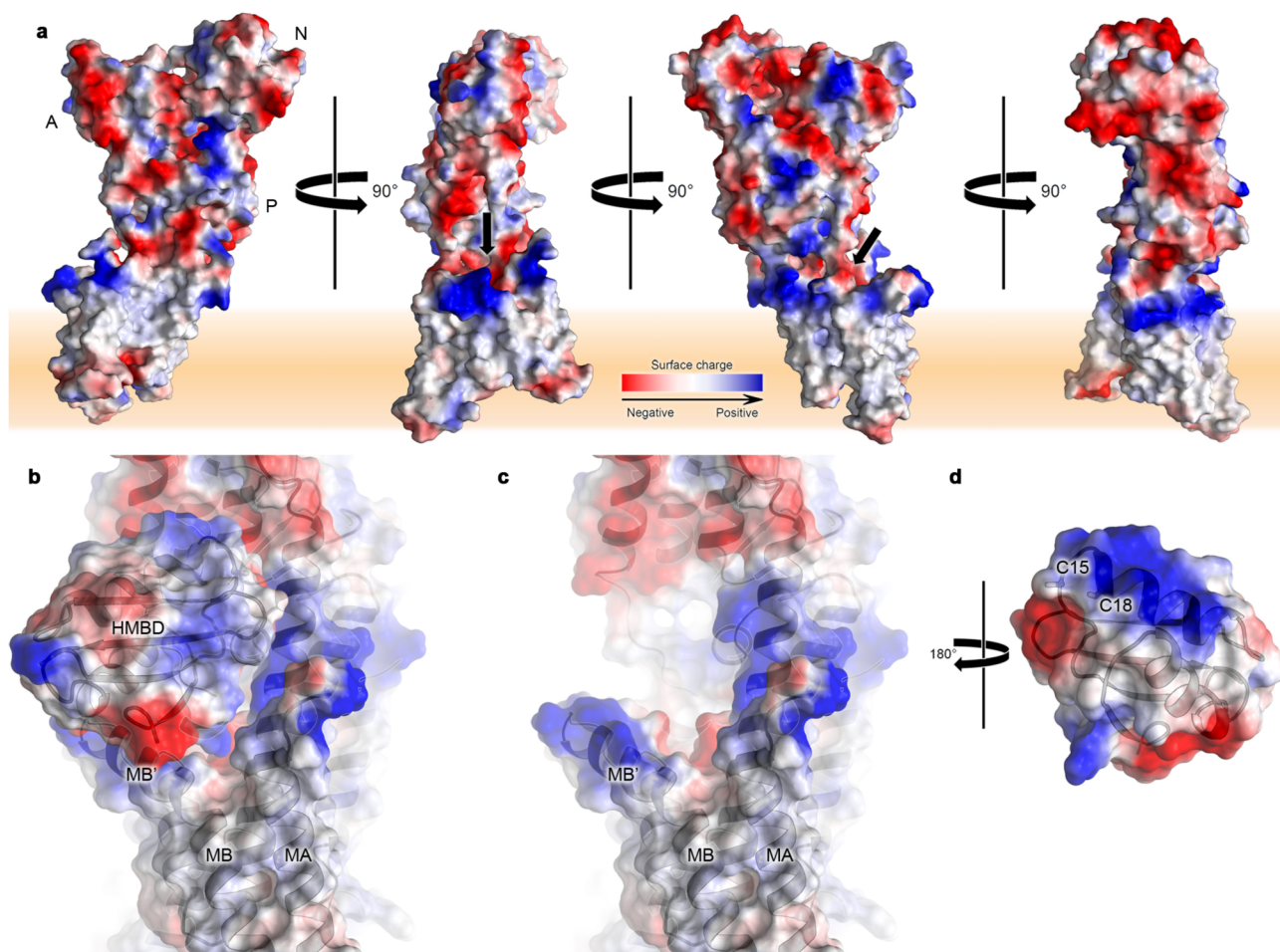
Extended Data Figure 6. The phosphorylation site of SsZntA

The domains are colored as in Fig. 1a. The $\text{AlF}_4^-/\text{BeF}_3^-$ (Al in orange, Be in green and F in cyan) and the Mg^{2+} ion (grey) are associated with Asp436 (in the DKTGT motif of the P-domain) at the interface between the A and P domains. Asp436, Thr438, Thr583, Asp628, Asn631 and Asp632 (in the P-domain) as well as Thr288, Gly289 and Glu290 (the TGE motif in the P-domain associated with dephosphorylation) are shown as sticks. Waters are shown as red spheres (not modeled for the E2P state). **a**, The E2P BeF_3^- -bound state. The catalytic Asp436 is protected from the TGE loop. **b**, The E2.P_i AlF_4^- -bound state. Glu279 of the TGE loop likely activates a water molecule for dephosphorylation as observed in the equivalent E2.P_i state of SERCA1a and CopA^{4,5,11}



Extended Data Figure 7. The extracellular pathway

a, The extracellular fraction of the E2-AlF₄⁻ crystal structure. Functionally important residues are shown as sticks, the protein is colored as in Fig. 1a and the final 2F_o-F_c electron density is contoured at 1σ. The view is equivalent to the one in Fig. 3d. **b**, Dynamics of Glu202 in 60 ns of MD simulation of the E2-BeF₃⁻ structure in a DOPC membrane in the absence of zinc. Selected residues are shown in sticks. Representatives of Glu202 conformations are captured at 16, 25 and 30 ns from snapshots aligned according to backbone C_α's of M1-M4. The orientation of Glu202 at 16 ns resembles how this side-chain looks in the E2-AlF₄⁻ state, while the flexibility observed throughout the simulation agrees with the poor observed electron density of the side chain in the E2-BeF₃⁻ state (see Fig. 3b). Note the two distorted lipids at the release pathway that may assist in Zn²⁺ release. **c**, Distance between the center of mass of C_γ of the Glu202 side-chain and N_Z of the Lys693 side-chain during the 60 ns simulations of the E2-ALF₄⁻ and E2-BeF₃⁻ SsZntA structures in the absence of zinc as a running average over five consecutive frames of each trajectory. **d**, The release pathway and accompanying protein interactions experienced by Zn²⁺ in a steered MD simulation originating from the center-of-mass of residues Cys392, Cys394 and Asp714. The TM domain, lipid phosphates, and water within 7 Å of the protein are colored as in panel b. **e**, The number of Zn²⁺-protein interactions with a 5 Å cut-off during steered MD simulations. Error bars correspond to counts from ten independent simulations with pulling speeds on Zn²⁺ ranging from 10–20 Å/ns.



Extended Data Figure 8. Surface charge distribution and docking of the HMBD to SzZntA
a, Overall structure in four different views of the E2-AlF₄⁻ structure. The view to the left is equivalent to Fig. 1a. The charge distribution complies with the positive-inside rule for membrane proteins⁵³. The putative ion entry funnel is highlighted with a black arrow. **b-d**, Docking of the HMBD to SsZntA. **b**, The apo-HMBD of EcZntA (PDB-ID 1MWY, Ref 13) docks to the entry site region of SsZntA using electrostatic complementation and van der Waals interactions, as predicted by the ClusPro 2.0 server³⁶. **c**, Equivalent view as in a of SsZntA without the HMBD. **d**, View of the isolated HMBD, rotated 180° relative to a to show the surface complementary to SsZntA. Ion-binding cysteines Cys15 and Cys18 are highlighted.

Extended Data Table 1

Data collection, phasing and refinement statistics.

Data collection ^a	E2.P ₁ [AlF ₄ ⁻]	E2P[BeF ₃ ⁻]	Se-E2.P ₁ [AlF ₄ ⁻]
Space group	C222 ₁	P2 ₁	C222 ₁
Cell dimensions			

a, b, c (Å)	77.6 83.6 319.8	54.5 61.0 141.5	76.1 82.2 314.8
α, β, γ (°)	90.0 90.0 90.0	90.0 96.0 90.0	90.0 90.0 90.0
Resolution, (Å) ^a	50-2.70 (2.80-2.70)	50-3.20 (3.30-3.20)	50-4.50 (4.62-4.50)
R_{merge} (%)	6.5 (126.7)	20.7 (115.3)	32.5 (99.1)
$I/\sigma I$	15.5 (1.04)	8.07 (1.37)	8.74 (3.40)
Completeness (%)	99.7 (93.2)	99.7 (99.8)	99.8 (99.0)
Redundancy	4.6 (4.6)	4.6 (4.8)	7.7 (7.8)
$CC(1/2)^b$ (%)	99.9 (73.5)	99.0 (56.8)	99.1 (84.3)
Refinement			
Resolution (Å)	50-2.70 (2.75-2.70)	50-3.20 (3.40-3.20)	
No. reflections	28862 (1294)	15448 (2437)	
$R_{\text{work}}/R_{\text{free}}$ (%)	20.7/24.0 (25.9/48.7)	21.0/28.1 (26.9/33.9)	
No. atoms			
Protein	4448	4347	
Ligand/ion	6	5	
Water	56	0	
B-factor			
Protein	77.9	92.4	
Ligand/ion	46.3	76.4	
Water	55.5		
R.m.s deviations			
Bond lengths (Å)	0.005	0.004	
Bond angles (°)	0.932	0.841	

^aHighest resolution shell is shown in parenthesis.

^b $CC_{1/2}$ values were calculated using XDS.

Extended Data Table 2

Statistical analysis of the ion entry region of SsZntA.

See also Figs. 3e,f. **a**, Conservation of the electronegative ion entry funnel in ZntA. The negative charges are provided in three blocks of surface exposed residues in helices M1 (182, 183, 184), M2 (210, 211, 214, 215) and M3 (345, 347, 348), in the vicinity of the negatively charged entry funnel of SsZntA. 521 ZntA-type proteins with less than 99 % sequence identity, selected from the latest UniProt database, were used for the analysis. **b**, Number of positively charged residues in the MB' helix of ZntA proteins using the same dataset as in a. **c**, Conservation of the CopA region equivalent to electronegative ion entry funnel in ZntA. Number of negatively charged residues in the MB' helix of CopA proteins. 617 CopA-type proteins with less than 95 % sequence identity, selected from the latest UniProt database, were used for the analysis.

a					
Block	Number of Asp + Glu in total	Number of sequences	Amino acid position	Number of Asp or Glu	Amino acid in SsZntA
M1	0	6	182	264	A
	1	357	183	227	I

a					
Block	Number of Asp + Glu in total	Number of sequences	Amino acid position	Number of Asp or Glu	Amino acid in SsZntA
	2	158	184	144	E
	3	0			
M2	0	35	210	0	F
	1	472	211	14	L
	2	14	214	485	E
	3	0	215	1	R
	4	0			
M3	0	234	345	4	R
	1	287	347	0	I
	2	0	348	283	D
	3	0			
All	0	0			
	1	8			
	2	155			
	3	328			
	4	30			
	5	0			

b	
Number of Lys + Arg in MB'	Number of sequences
0	0
1	18
2	130
3	308
4	58
5	6
6	1

c					
Block	Number of Asp + Glu in total	Number of sequences	Amino acid position	Number of Asp or Glu	Amino acid in LpCopA
M1	0	617	153	0	A
	1	0	154	0	M
	2	0	155	0	G
	3	0			
M2	0	608	198	0	V
	1	8	199	1	L
	2	0	202	7	Q

c					
Block	Number of Asp + Glu in total	Number of sequences	Amino acid position	Number of Asp or Glu	Amino acid in LpCopA
	3	0	203	0	V
	4	0			
M3	0	31	334	25	R
	1	560	336	1	A
	2	26	337	586	D
	3	0			
All	0	31			
	1	552			
	2	34			
	3	0			
	4	0			
	5	0			

Acknowledgments

We thank J. L. Karlsen for support on crystallographic computing. O.S. and H.E.A. are supported by the Graduate School of Science and Technology at Aarhus University. G.M. is supported by a Marie Curie International Outgoing Fellowship (European Commission, grant no. 252961). MA was supported by a Marie Curie Career Integration Grant (FP7-MC-CIG-618558). P.N. was supported by an advanced research grant of the European Research Council (grant no. 250322 Biomemos) and P.G. at later stages by the Lundbeck Foundation. We are grateful for assistance with crystal screening at Maxlab, Lund, Sweden, beam lines 911-2/3, and data collection at the Swiss Light Source, the Paul Scherrer Institute, Villigen, beam line X06SA. Access to synchrotron sources was supported by the Danscatt program of the Danish Council of Independent Research, and by BioStruct-X contract 860.

References

- Berg JM, Shi Y. The galvanization of biology: a growing appreciation for the roles of zinc. *Science*. 1996; 271:1081–1085. [PubMed: 8599083]
- Williams LE, Mills RF. P(1B)-ATPases--an ancient family of transition metal pumps with diverse functions in plants. *Trends Plant Sci*. 2005; 10:491–502. [PubMed: 16154798]
- Arguello JM, Gonzalez-Guerrero M, Raimunda D. Bacterial transition metal P(1B)-ATPases: transport mechanism and roles in virulence. *Biochemistry*. 2011; 50:9940–9949. [PubMed: 21999638]
- Olesen C, et al. The structural basis of calcium transport by the calcium pump. *Nature*. 2007; 450:1036–U1035. [PubMed: 18075584]
- Toyoshima C, Norimatsu Y, Iwasawa S, Tsuda T, Ogawa H. How processing of aspartylphosphate is coupled to lumenal gating of the ion pathway in the calcium pump. *Proc Natl Acad Sci U S A*. 2007; 104:19831–19836. [PubMed: 18077416]
- Laursen M, Yatime L, Nissen P, Fedosova NU. Crystal structure of the high-affinity Na⁺K⁺-ATPase-ouabain complex with Mg²⁺ bound in the cation binding site. *Proc Natl Acad Sci U S A*. 2013; 110:10958–10963. [PubMed: 23776223]
- Domingo JL. Metal-induced developmental toxicity in mammals: a review. *J Toxicol Environ Health*. 1994; 42:123–141. [PubMed: 8207750]
- Counago RM, et al. Imperfect coordination chemistry facilitates metal ion release in the Psa permease. *Nature chemical biology*. 2014; 10:35–41.

9. Albers RW. Biochemical aspects of active transport. *Annu Rev Biochem.* 1967; 36:727–756. [PubMed: 18257736]
10. Raimunda D, Subramanian P, Stemmler T, Arguello JM. A tetrahedral coordination of Zinc during transmembrane transport by P-type Zn(2+)-ATPases. *Biochim Biophys Acta.* 2012; 1818:1374–1377. [PubMed: 22387457]
11. Gourdon P, et al. Crystal structure of a copper-transporting PIB-type ATPase. *Nature.* 2011; 475:59–64. [PubMed: 21716286]
12. Andersson M, et al. Copper-transporting P-type ATPases use a unique ion-release pathway. *Nature structural & molecular biology.* 2014; 21:43–48.
13. Banci L, et al. A new zinc-protein coordination site in intracellular metal trafficking: solution structure of the Apo and Zn(II) forms of ZntA(46–118). *J Mol Biol.* 2002; 323:883–897. [PubMed: 12417201]
14. Gourdon P, et al. HiLiDe-Systematic Approach to Membrane Protein Crystallization in Lipid and Detergent. *Cryst Growth Des.* 2011; 11:2098–2106.
15. Okkeri J, Haltia T. The metal-binding sites of the zinc-transporting P-type ATPase of *Escherichia coli*. Lys693 and Asp714 in the seventh and eighth transmembrane segments of ZntA contribute to the coupling of metal binding and ATPase activity. *Biochim Biophys Acta.* 2006; 1757:1485–1495. [PubMed: 16890908]
16. Patel K, Kumar A, Durani S. Analysis of the structural consensus of the zinc coordination centers of metalloprotein structures. *Biochim Biophys Acta.* 2007; 1774:1247–1253. [PubMed: 17855175]
17. Andreini C, Bertini I, Cavallaro G. Minimal functional sites allow a classification of zinc sites in proteins. *PLoS One.* 2011; 6:e26325. [PubMed: 22043316]
18. Pedersen BP, Buch-Pedersen MJ, Morth JP, Palmgren MG, Nissen P. Crystal structure of the plasma membrane proton pump. *Nature.* 2007; 450:1111–1114. [PubMed: 18075595]
19. Faxen K, et al. Characterization of a *Listeria monocytogenes* Ca(2+) pump: a SERCA-type ATPase with only one Ca(2+)-binding site. *J Biol Chem.* 2011; 286:1609–1617. [PubMed: 21047776]
20. Clausen JD, Andersen JP. Glutamate 90 at the luminal ion gate of sarcoplasmic reticulum Ca2+-ATPase is critical for Ca(2+) binding on both sides of the membrane. *J Biol Chem.* 2010; 285:20780–20792. [PubMed: 20421308]
21. Zhitnitsky D, Lewinson O. Identification of functionally important conserved trans-membrane residues of bacterial PIB -type ATPases. *Molecular microbiology.* 2014; 91:777–789. [PubMed: 24350798]
22. Winther AM, et al. The sarcolipin-bound calcium pump stabilizes calcium sites exposed to the cytoplasm. *Nature.* 2013; 495:265–269. [PubMed: 23455424]
23. Toyoshima C, et al. Crystal structures of the calcium pump and sarcolipin in the Mg2+-bound E1 state. *Nature.* 2013; 495:260–264. [PubMed: 23455422]
24. Ekberg K, Wielandt AG, Buch-Pedersen MJ, Palmgren MG. A conserved asparagine in a P-type proton pump is required for efficient gating of protons. *J Biol Chem.* 2013; 288:9610–9618. [PubMed: 23420846]
25. Lee JY, Yang JG, Zhitnitsky D, Lewinson O, Rees DC. Structural basis for heavy metal detoxification by an Atm1-type ABC exporter. *Science.* 2014; 343:1133–1136. [PubMed: 24604198]
26. Gonzalez-Guerrero M, Arguello JM. Mechanism of Cu+-transporting ATPases: soluble Cu+ chaperones directly transfer Cu+ to transmembrane transport sites. *Proc Natl Acad Sci U S A.* 2008; 105:5992–5997. [PubMed: 18417453]
27. Mattle D, et al. On Allosteric Modulation of P-Type Cu-ATPases. *J Mol Biol.* 2013
28. Padilla-Benavides T, McCann CJ, Arguello JM. The mechanism of Cu+ transport ATPases: interaction with CU+ chaperones and the role of transient metal-binding sites. *J Biol Chem.* 2013; 288:69–78. [PubMed: 23184962]
29. Dutta SJ, Liu J, Stemmler AJ, Mitra B. Conservative and nonconservative mutations of the transmembrane CPC motif in ZntA: effect on metal selectivity and activity. *Biochemistry.* 2007; 46:3692–3703. [PubMed: 17326661]

30. Chovancova E, et al. CAVER 3.0: a tool for the analysis of transport pathways in dynamic protein structures. *PLoS computational biology*. 2012; 8:e1002708. [PubMed: 23093919]
31. Kabsch W. Xds. *Acta Crystallogr D Biol Crystallogr*. 2010; 66:125–132. [PubMed: 20124692]
32. McCoy AJ, et al. Phaser crystallographic software. *J Appl Crystallogr*. 2007; 40:658–674. [PubMed: 19461840]
33. Emsley P, Lohkamp B, Scott WG, Cowtan K. Features and development of Coot. *Acta Crystallogr D Biol Crystallogr*. 2010; 66:486–501. [PubMed: 20383002]
34. Afonine PV, et al. Towards automated crystallographic structure refinement with phenix.refine. *Acta Crystallogr D Biol Crystallogr*. 2012; 68:352–367. [PubMed: 22505256]
35. Baginski ES, Foa PP, Zak B. Microdetermination of inorganic phosphate, phospholipids, and total phosphate in biologic materials. *Clin Chem*. 1967; 13:326–332. [PubMed: 6036717]
36. Kozakov D, et al. Achieving reliability and high accuracy in automated protein docking: ClusPro, PIPER, SOU, and stability analysis in CAPRI rounds 13–19. *Proteins-Structure Function and Bioinformatics*. 2010; 78:3124–3130.
37. Yang W, Gao YQ, Cui Q, Ma J, Karplus M. The missing link between thermodynamics and structure in F1-ATPase. *Proc Natl Acad Sci U S A*. 2003; 100:874–879. [PubMed: 12552084]
38. Damjanovic A, Garcia-Moreno EB, Brooks BR. Self-guided Langevin dynamics study of regulatory interactions in NtrC. *Proteins*. 2009; 76:1007–1019. [PubMed: 19384996]
39. Lomize MA, Lomize AL, Pogozheva ID, Mosberg HI. OPM: orientations of proteins in membranes database. *Bioinformatics*. 2006; 22:623–625. [PubMed: 16397007]
40. Phillips JC, et al. Scalable molecular dynamics with NAMD. *J Comput Chem*. 2005; 26:1781–1802. [PubMed: 16222654]
41. MacKerell AD, et al. All-atom empirical potential for molecular modeling and dynamics studies of proteins. *Journal of Physical Chemistry B*. 1998; 102:3586–3616.
42. Klauda JB, et al. Update of the CHARMM all-atom additive force field for lipids: validation on six lipid types. *J Phys Chem B*. 2010; 114:7830–7843. [PubMed: 20496934]
43. Martyna GJ, Tobias DJ, Klein ML. Constant-Pressure Molecular-Dynamics Algorithms. *Journal of Chemical Physics*. 1994; 101:4177–4189.
44. Feller SE, Zhang YH, Pastor RW, Brooks BR. Constant-Pressure Molecular-Dynamics Simulation - the Langevin Piston Method. *Journal of Chemical Physics*. 1995; 103:4613–4621.
45. Essmann U, et al. A Smooth Particle Mesh Ewald Method. *Journal of Chemical Physics*. 1995; 103:8577–8593.
46. Sotomayor M, Schulten K. Single-molecule experiments in vitro and in silico. *Science*. 2007; 316:1144–1148. [PubMed: 17525328]
47. Izrailev S, Stepaniants S, Balsera M, Oono Y, Schulten K. Molecular dynamics study of unbinding of the avidin-biotin complex. *Biophys J*. 1997; 72:1568–1581. [PubMed: 9083662]
48. Schrodinger LLC. The PyMOL Molecular Graphics System, Version 1.3r1. 2010
49. Wu CC, et al. The cadmium transport sites of CadA, the Cd²⁺-ATPase from *Listeria monocytogenes*. *Journal of Biological Chemistry*. 2006; 281:29533–29541. [PubMed: 16835223]
50. Post RL, Kume S, Hegyvary C. Activation by Adenosine-Triphosphate in Phosphorylation Kinetics of Sodium and Potassium Ion Transport Adenosine-Triphosphatase. *Journal of Biological Chemistry*. 1972; 247:6530. [PubMed: 4263199]
51. Braberg H, et al. SALIGN: a web server for alignment of multiple protein sequences and structures. *Bioinformatics*. 2012; 28:2072–2073. [PubMed: 22618536]
52. Sharma R, Rensing C, Rosen BP, Mitra B. The ATP hydrolytic activity of purified ZntA, a Pb(II)/Cd(II)/Zn(II)-translocating ATPase from *Escherichia coli*. *J Biol Chem*. 2000; 275:3873–3878. [PubMed: 10660539]
53. von Heijne G. The distribution of positively charged residues in bacterial inner membrane proteins correlates with the trans-membrane topology. *EMBO J*. 1986; 5:3021–3027. [PubMed: 16453726]

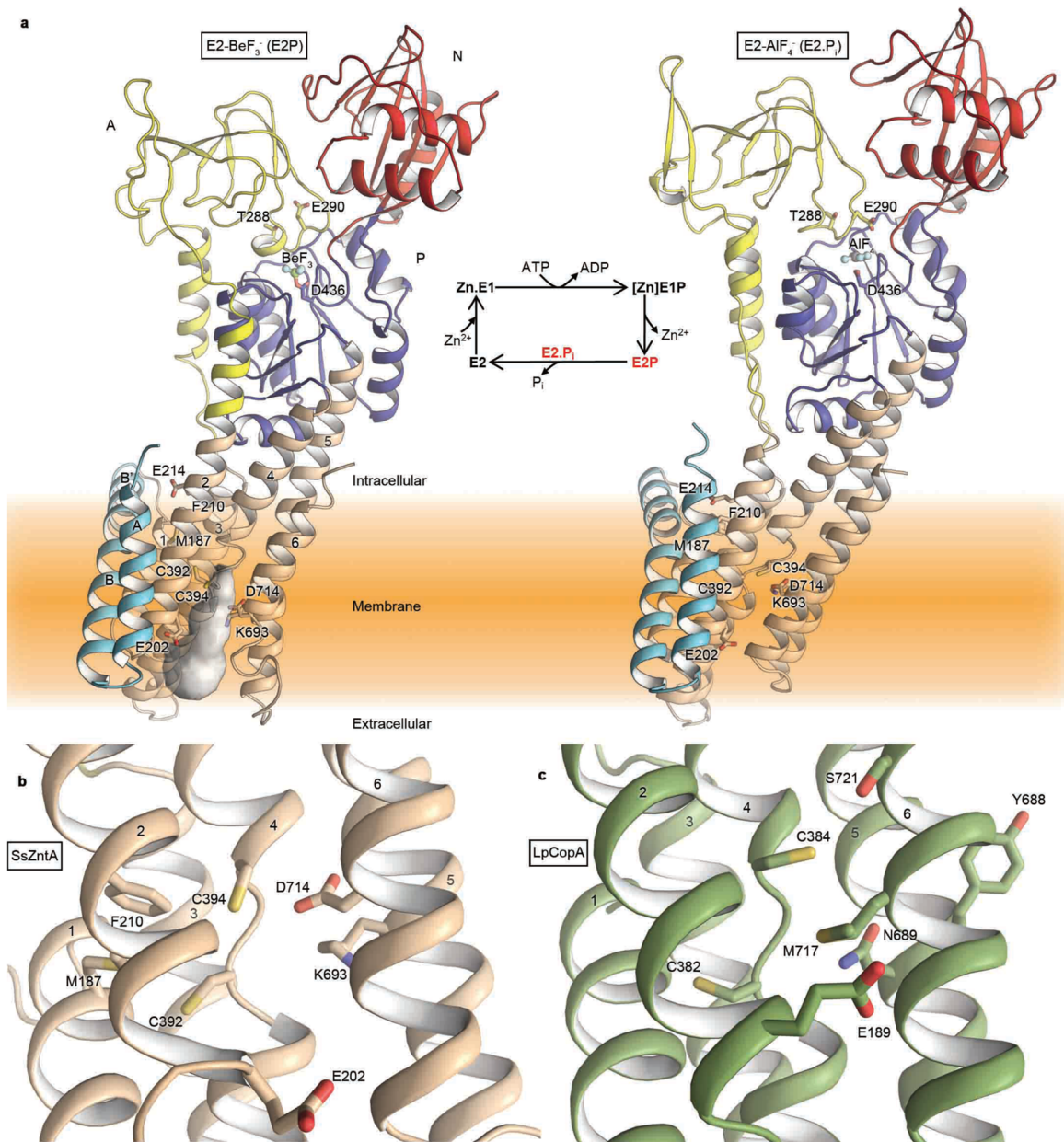


Figure 1. Structures of the *S. sonnei* Zn^{2+} -ATPase

a, The E2- BeF_3^- (E2P, left) and E2- AlF_4^- (E2.P_i, right) structures with class-specific helices MA, MB and MB' colored cyan, helices M1-M6 colored wheat and the A-, P- and N-domains colored yellow, blue and red, respectively. Key residues for function are highlighted. An extracellular release pathway (white surface) is present only in the E2P state as computed with CAVER³⁰. The inset shows a schematic Post-Albers reaction cycle⁹ for ZntA, with the experimentally determined structures marked in red. **b**, Close-view of the intramembranous ion-binding region colored as in Fig. 1a displaying the proposed Zn^{2+} -binding residues Cys392 and Cys394 (in M4), Lys693 (M5) and Asp714 (M6)^{10,15}. **c**, Equivalent view as in Fig. 1b of the Cu^+ -ATPase LpCopA (PDB-ID 3RFU, Ref 11). Critical

CopA residues overlay with equally important residues of Zn²⁺-ATPases. See also Extended Data Fig. 2.

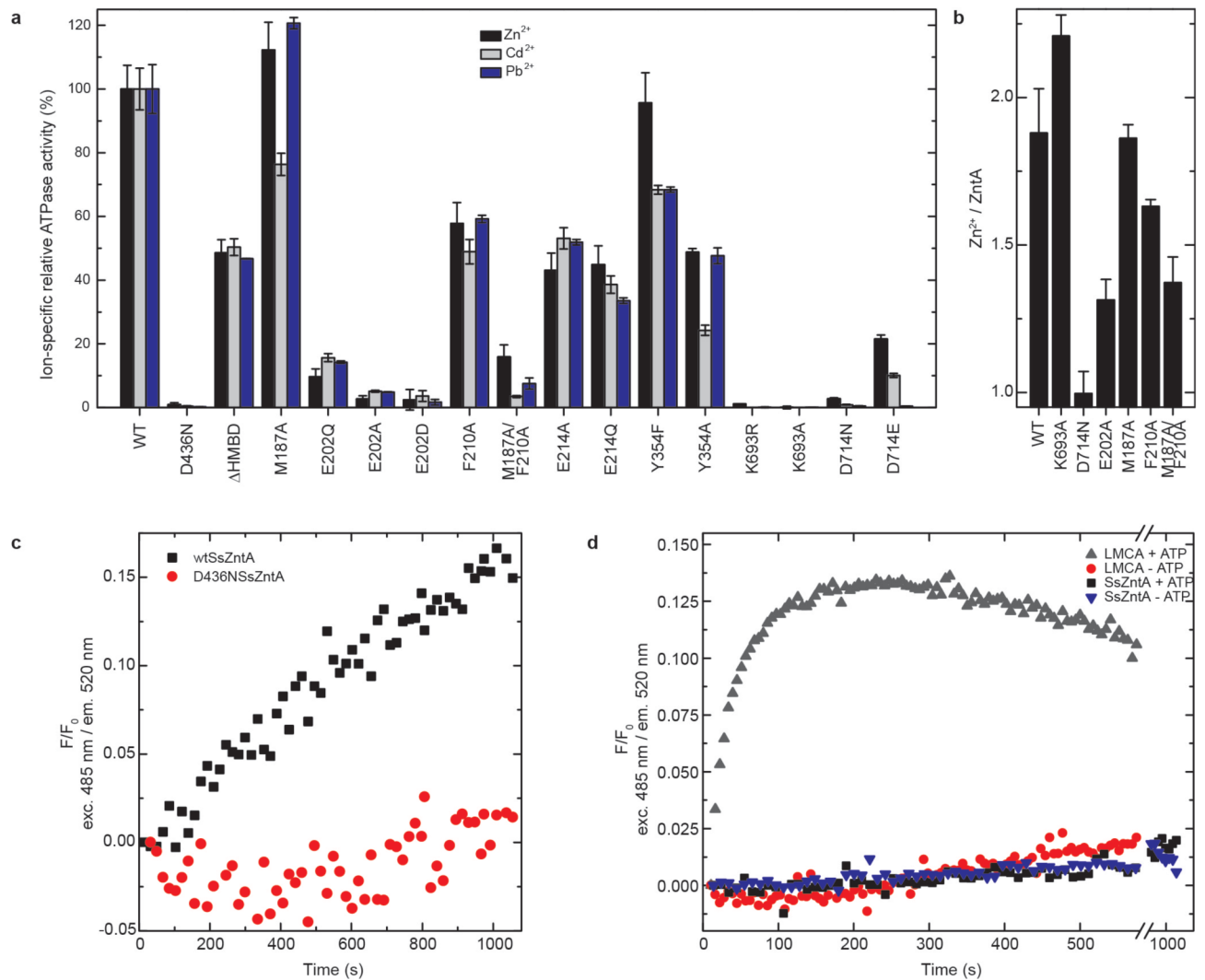


Figure 2. Functional studies of zinc, cadmium, lead and counter-ion transport in SsZntA
a, ATP turn-over associated with different SsZntA constructs in detergent-lipid solution. The specific activity for wild-type SsZntA with Zn²⁺, Cd²⁺ and Pb²⁺ were 592±23, 491±10 and 813±23 nmol P_i mg⁻¹ min⁻¹, respectively. Technical average and s.d. (n=3). **b**, Zn²⁺-binding to different SsZntA constructs as determined using the dye Zincon. ZntA binds two Zn²⁺ ions, one to the high-affinity site in the TM domain and one to the HMBD. Biological average and s.d. (n=3). **c,d** Zinc transport (of wild-type and Asp436Asn SsZntA proteoliposomes, respectively) and measurements of proton counter-ion transport (for wild-type SsZntA and Ca²⁺-ATPase LMCA proteoliposomes, respectively) monitored using the zinc-selective chelator FluoZin-1 and the pH indicator pyranine, respectively. See also Extended Data Fig. 4d.

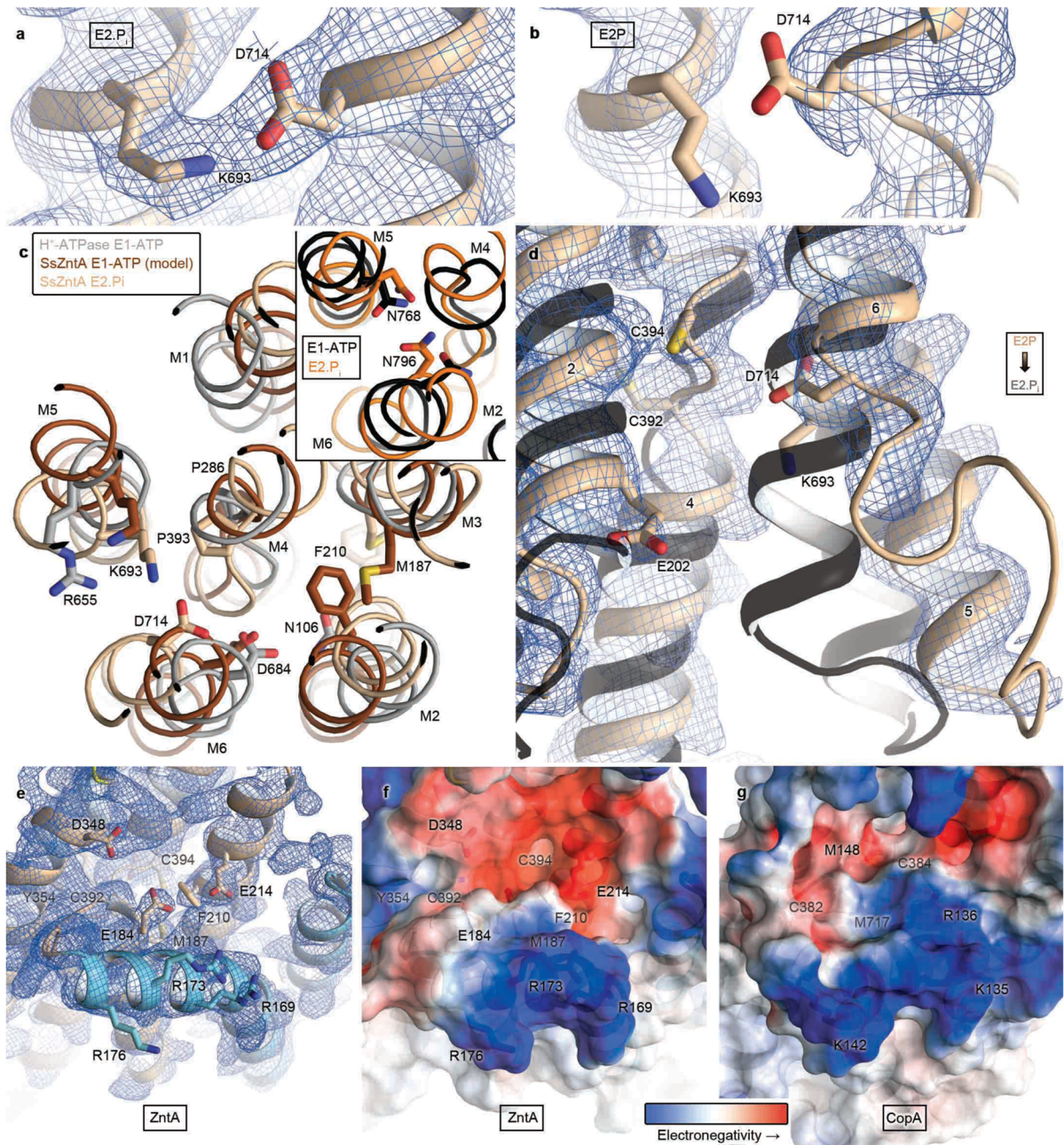


Figure 3. Details of the ZntA structures

Blue mesh represents the final $2F_o - F_c$ electron density, contoured at 1σ and see Methods for additional figure details. **a**, E2.P_i state close-view of Lys693 and Asp714. **b**, E2P state close-view of Lys693 and Asp714. **c**, Comparison of the transmembrane regions of SsZntA-AIF₄⁻ (colored as in Fig. 1a), *Arabidopsis thaliana* AHA2 H⁺-ATPase (in the E1-ATP state, PDB-ID 3B8C, Ref 18, colored in grey) and an E1-ATP model of SsZntA (in brown). Inset: identical view of the equivalent region of the E1-ATP (black) and E2.P_i (orange) states of SERCA (PDB-IDs 1T5S and 3B9R). **d**, Structural differences between the extracellular

portions of the E2P (colored as in Fig. 1a) and the E2.P_i structures (black). See also Extended Data Fig. 7a. **e,f,g**, The MB' platform of SsZntA (e,f) and LpCopA (g).

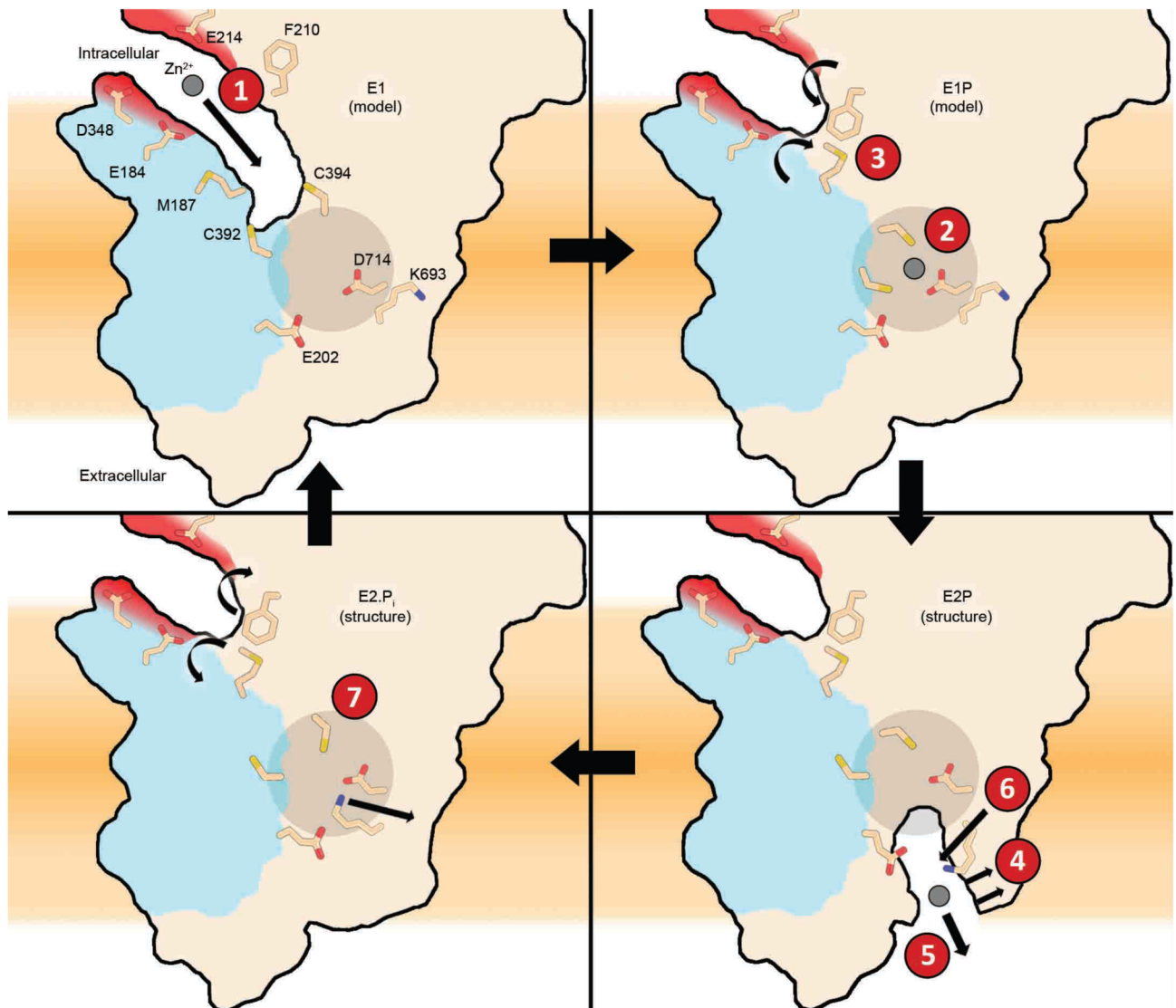


Figure 4. Putative zinc transport mechanism for ZntA

A transport cycle based on schematic models of the E1 and E1P states and the E2P and E2.P_i structures. In the presence of intracellular zinc, Zn²⁺ enters the ATPase through the electronegative funnel (red) at the MB' platform (1). Upon Zn²⁺-binding (2) to the intramembranous ion-binding site (grey circle), Phe210 and Met187 occlude the ion entry funnel (3), preventing backflow of Zn²⁺. Substantial domain rearrangements in transition to the E2P state open the extracellular pathway (4), lowering the Zn²⁺-affinity and mediating Zn²⁺ release (5), possibly stimulated by Lys693 (6). Dephosphorylation triggers closure of the transmembrane domain, where Lys693 as a built-in counter-ion forms a salt bridge with Asp714. Upon dephosphorylation, the side-chains move to their initial positions (7) prior to an E2-E1 transition stimulated by intracellular Zn²⁺.